

# Self-Powered Dual-Mode Amenity Sensor Based on the Water–Air Triboelectric Nanogenerator

Hao Wang,<sup>†,‡,§,||</sup> Han Wu,<sup>†</sup> Dihan Hasan,<sup>†,‡,§,||</sup> Tianyiyi He,<sup>†,‡,§,||</sup> Qiongfeng Shi,<sup>†,‡,§,||</sup> and Chengkuo Lee<sup>\*,†,‡,§,||</sup>

<sup>†</sup>Department of Electrical and Computer Engineering, National University of Singapore, 4 Engineering Drive 3, Singapore 117583

<sup>‡</sup>Center for Intelligent Sensors and MEMS, National University of Singapore, E6 #05-11F, 5 Engineering Drive 1, Singapore 117608

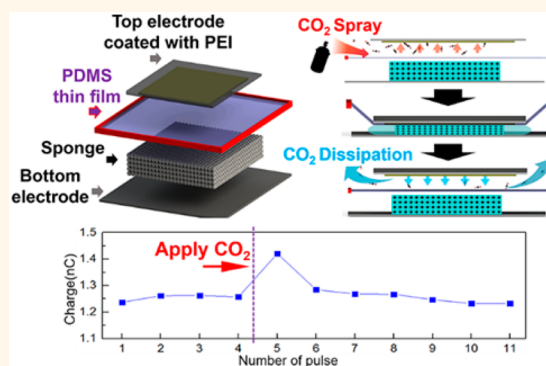
<sup>§</sup>Hybrid-Integrated Flexible (Stretchable) Electronic Systems Program, National University of Singapore, E6 #05-4, 5 Engineering Drive 1, Singapore 117608

<sup>||</sup>NUS Suzhou Research Institute (NUSRI), Suzhou, Industrial Park, Suzhou, P. R. China 215123

## Supporting Information

**ABSTRACT:** A water–air triboelectric nanogenerator (WATENG) is presented for CO<sub>2</sub> sensing application. During the operation of WATENG, two independent charge transfers can be used to characterize the effect of force and humidity, respectively. Thus, the structure of WATENG provides a capability to eliminate these two major interferences in a triboelectric self-powered sensor. With the aid of the polyethylenimine (PEI) coating, WATENG can be used for CO<sub>2</sub> sensing in both static and dynamic conditions. In static condition with a stable CO<sub>2</sub> concentration, the CO<sub>2</sub> sensing is characterized with respect to different relative humidity, and the sensing range can be up to 6000 ppm. In dynamic CO<sub>2</sub> sensing of a pulse gas spray, due to the fast recovery of PEI surface reaction, the sensing range of dynamic situation can be broadened to 30,000 ppm. The self-powered and portable feature of WATENG is preferable as a self-powered amenity sensor for the construction of internet of the things (IoT) sensor networks in the future.

**KEYWORDS:** portable, CO<sub>2</sub> sensing, humidity calibration, force free, charge-based characterization



Modern smart buildings provide amenities to users with the aid of advanced demand-controlled heating ventilation air conditioning (HVAC) systems,<sup>1</sup> where it requires advanced sensor networks to control the parameters such as temperature, humidity, and CO<sub>2</sub> concentration. By leveraging the MEMS technology, a few amenity sensors of minimized dimension are developed to fit requirements of the sensor networks.<sup>2–7</sup> However, one of the essential issues that cannot be bypassed is the power consumption of present commercial amenity sensors. Taking the CO<sub>2</sub> monitor, the main indicator of indoor air quality (IAQ), as an example, the information on air flow at different locations in a large indoor space (such as office floor, ballroom, auditorium, and lobby, etc.) needs to be collected in a real-time manner such that the individually controlled dampers in this large indoor space can separately regulate the distribution of air-flow. For the construction of large-scale sensor networks and internet of the things (IoT) sensor networks used in smart buildings in the future, the sensor nodes in the system need to have the capability of operating independently, sustainably, and

maintenance-free. Otherwise, because massive sensor nodes are distributed within the entire area, periodic replacement of batteries in sensor nodes is a labor intensive task and will create a significant amount of waste materials from batteries, as they are environmentally unfriendly and potentially hazardous to human health.<sup>8</sup> Therefore, self-powered sensor nodes are crucial for enabling a sensor network without using batteries.<sup>9,10</sup>

In the past decade, triboelectric nanogenerators (TEGs) show the great potential for applications in mechanical energy harvesters and self-powered sensors.<sup>11–19</sup> The versatile nature of TENGs enables the capability of sensing all parameters that are relevant to the factors affecting the performance such as force, frequency, and surface charge density. Recently, various types of triboelectric-based sensors have been investigated such as the pressure sensor,<sup>20–25</sup> vibration sensor,<sup>26–29</sup> motion

Received: July 23, 2017

Accepted: October 2, 2017

Published: October 2, 2017

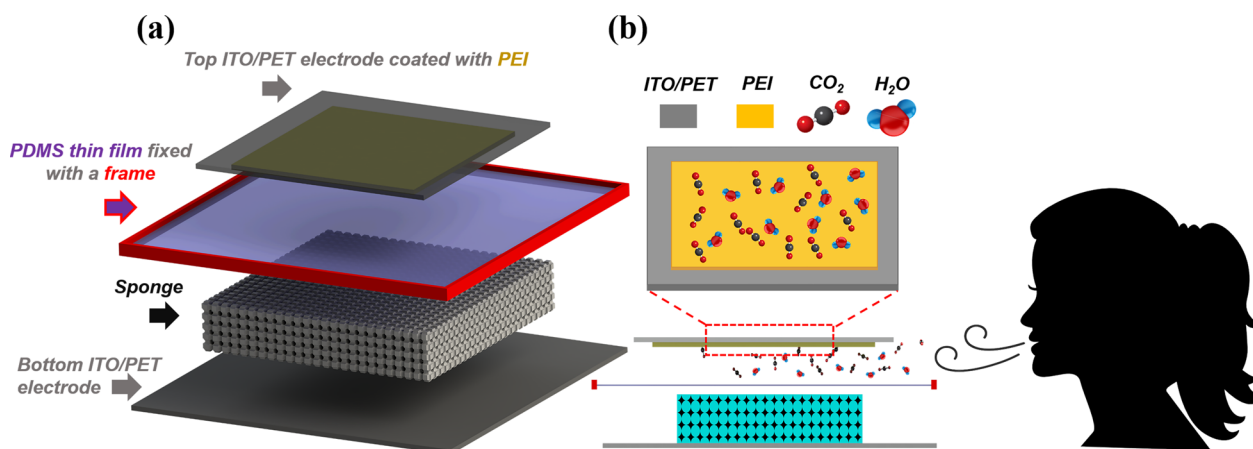


**Figure 1.** (a) Illustration of the WATENG layer structure. (b) Schematic diagram that shows the concept of the WATENG-based CO<sub>2</sub> sensor, which is comprised of a PEI layer with an interference of humidity.

sensor,<sup>30–32</sup> liquid sensor,<sup>33,34</sup> and chemical/environmental sensor.<sup>35–40</sup> However, the versatile nature of the triboelectric sensor also means that more interference will be introduced with the application of sensing a specific parameter. One critical issue reported in usage of the triboelectric sensor is the interference of humidity. Water vapor in air will affect the generation of electrostatic charge, which is the key factor for contact electrification in triboelectric sensors. The previous study confirms that the humidity fluctuation within a small range can induce a large variation of the triboelectric output.<sup>41–43</sup> Therefore, a proper calibration or even elimination of humidity effect is necessary to enhance the sensing accuracy of triboelectric-based sensors.

So far, several kinds of triboelectric chemical sensors have been investigated, such as Hg<sup>2+</sup> ion sensing<sup>35</sup> and catechin sensing,<sup>36</sup> however, gas sensing is still a rarely touched field. A preliminary study reports a stacked corrugated-core sandwich-structured TENG for H<sub>2</sub> sensing.<sup>40</sup> Although the detailed sensing mechanism still remains unknown and the result shows no sensing selectivity to other gas species, it reveals a gas sensing feasibility by triboelectric mechanism. In this study, a polyethylenimine (PEI) layer was used as the CO<sub>2</sub> selective sensing material incorporated in TENG gas sensors. Hence, it becomes possible to develop a TENG gas sensor with high sensing selectivity by having a special functional coating on top of the triboelectric layer, where only a specific gas molecule can alter the surface property of that functional material. Compared with current CO<sub>2</sub> sensors,<sup>44–48</sup> PEI can avoid the issues of cross-sensitivity, long response time, poor reversibility, and poor sensitivity which are mainly introduced by imperfect sensing material properties.<sup>46–48</sup> In the previous study, only the infrared investigation of CO<sub>2</sub> bulk absorption in the PEI layer was conducted for measuring the CO<sub>2</sub> concentration.<sup>44,45</sup> By investigating the change of the surface charge of PEI with CO<sub>2</sub> absorption, a simple triboelectrification process can replace the desktop FTIR equipment for CO<sub>2</sub> detection.

Here we propose a water–air triboelectric nanogenerator (WATENG) as a portable CO<sub>2</sub> sensing device. Meanwhile, the effect of humidity for CO<sub>2</sub> sensing using PEI is calibrated. This is a preliminary study that investigates how water molecules affect surface charge density so as to enable self-generated triboelectric-based gas detection from the output charge.

## RESULTS AND DISCUSSION

**WATENG Mechanism Analysis and Output Characterization.** Figure 1a shows a device configuration in the WATENG for CO<sub>2</sub> detection. This WATENG is comprised of a top air layer and a bottom wetted sponge layer that is separated via a suspended PDMS thin film at the center. The contact electrification between the top electrode and the upper surface of PDMS has a constant contact area with a mutative humidity of the ambient environment. For the contact electrification between the lower surface of PDMS and wetted sponge, this contact area is a function of applied force where the humidity is kept at a maximum and stable. Thus, during the operation, there will be two independent charge-transfer mechanisms: One is not affected by force, and another is not affected by humidity. Hence, humidity and force can be characterized independently. In a previous investigation of triboelectric-based sensors, a force control system is required for a stable operation force to induce contact and separation.<sup>20–40</sup> This force control system makes the entire sensing system not portable. Therefore, TENGs can generate a stable output with varied force or even directly measure the force, which is essential for developing portable self-powered chemical sensors operated manually.

The CO<sub>2</sub> sensing concept is shown in Figure 1b. The PEI coating on the top electrode can absorb CO<sub>2</sub> and further change the electronegativity of its surface. Hence, the change of the triboelectric output can be used to measure the CO<sub>2</sub> concentration. For most cases, the change in CO<sub>2</sub> concentration is usually accompanied by a change of relative humidity (RH), for example, during exhalation. The effect of gaseous water in CO<sub>2</sub> sensing is characterized in this study.

The detailed WATENG structure is shown in Figure 1a. The entire device includes four layers. The top and bottom ITO/PET electrodes act as the electrode pair of the device. The PEI layer, which is a type of macromolecule for CO<sub>2</sub> adsorbents, was dip-coated onto the top ITO/PET electrode. A sponge is located at the center of the bottom ITO/PET electrode. During the operation, the sponge is wetted with water, then the water can be squeezed out. This function plays an important role for force sensing and output enhancement. The PDMS thin film, which is located between the sponge and the top ITO/PET electrode, is fixed and stretched by a frame to provide contact electrification between the two top electrodes and triboelectric charge due to water being squeezed out from the sponge. A

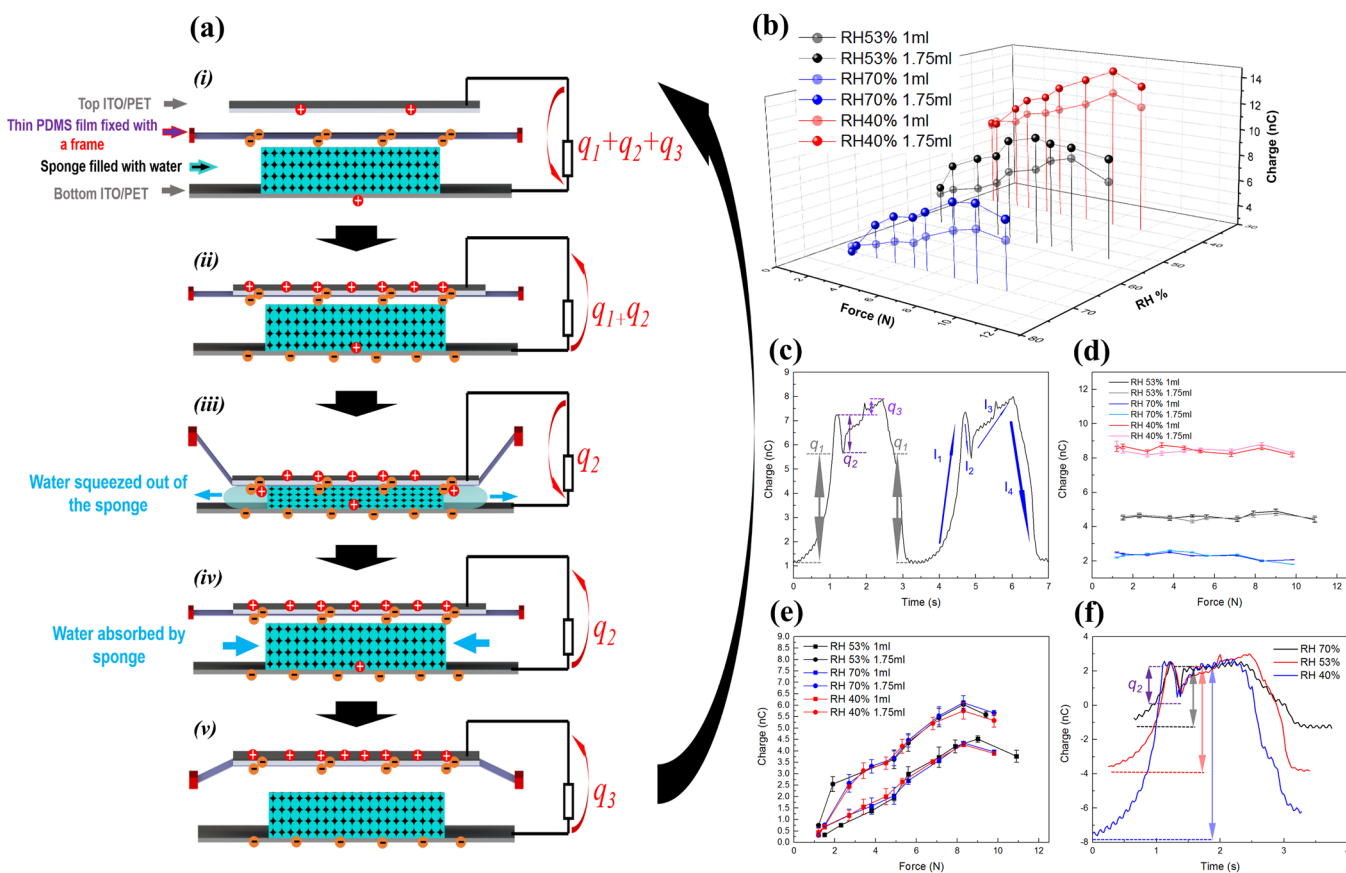


**Figure 2.** (a) Working mechanism of the WANTENG. (b) The total charge transferred with different RH, force and water volume. (c) A typical charge curve during the operation. (d) The value of  $q_1$  with different RH, force, and water volume. (e) The value of  $q_2$  with different RH, force, and water volume. (f) A group of charge curves showing  $q_2$  was not affected by RH (force = 2.7 N; water volume = 1.75 mL).

detailed fabrication process and optical and SEM images of the WANTENG can be found in [Supplementary S1](#).

**Working Mechanism of WANTENG with PEI for Gas Sensing.** The working mechanism is illustrated in [Figure 2a](#). The entire operation will induce a charge flow cycle, as shown in [Figure 2c](#). After the first cycle of operation, the suspended PDMS thin film obtains negative electrostatic charges on both the upper surface, which is  $q_1$ , and the lower surface, which is  $q_2$ , as shown in [Figure 2a-i](#). In this step, the top ITO/PET electrode is separated from the PDMS thin film. Then, the ITO/PET electrode is pressed to produce a contact with the PDMS thin film, as shown in [Figure 2a-ii](#). Due to the contact between ITO and PDMS surface, the negative electrostatic charges on both sides of the PDMS thin film will be balanced by the positive charge on the ITO/PET electrode, inducing a charge flow, which is  $q_1 + q_2$ , from the bottom ITO/PET electrode to the top ITO/PET electrode, which is indicated as  $I_1$  in [Figure 2c](#). Then, we further press the top electrode to deform the suspended PDMS thin film and compress the wetted sponge, as shown in [Figure 2a-iii](#). In this step, the water within the wetted sponge will be squeezed out from the sponge and contact the lower surface of the PDMS thin film. Hence, the negative electrostatic charge on the lower surface of the PDMS thin film,  $q_2$ , which is initially balanced by the positive charge on the top electrode, will be coupled by positive ions in water, which will form a so-called electric double layer. During this step, a charge flow from the top electrode to the bottom electrode will be induced, indicated as  $I_2$  in [Figure 2c](#). Then, the top electrode is lifted up to make the sponge absorb all of the

water back, as shown in [Figure 2a-iv](#). Again, without the electric double layer being formed by the contact between water and the lower surface of PDMS, the negative electrostatic charge on the lower surface of the PDMS thin film will be balanced by the positive charge on the top electrode, which induces a charge flow  $q_2$  from the bottom electrode to the top electrode. Due to the sticky surface of PDMS, PDMS can be lifted up together with the top electrode to a certain height before the complete separation occurs, as shown in [Figure 2a-iv](#). In this step, the distance between the bottom electrode and PDMS thin film is increasing, which will further lower the electrostatic induction between them. Thus, a very small charge flow,  $q_3$ , from the bottom electrode to the top electrode will occur. During the entire lifting up process, a charge flow, indicated as  $I_3$ , which is comprised of  $q_2$  and  $q_3$  in [Figure 2c](#), will occur. If the top electrode is further lifted up, PDMS will completely separate from the top electrode, making the entire device recover to the initial status as shown in [Figure 2a-i](#). The negative electrostatic charge on both sides of the PDMS thin film will be balanced by the entire environment, and a charge flow of  $I_4$ , which is comprised of  $q_1$ ,  $q_2$ , and  $q_3$ , from the top electrode to the bottom electrode will occur, as indicated in [Figure 2c](#).

As explained in the working mechanism, the charge transfer in the entire cycle is determined by the negative electrostatic charge on both sides of the PDMS thin film. The total negative electrostatic charge should be the sum of  $q_1$ ,  $q_2$ , and  $q_3$ . Among them,  $q_3$  refers to the change of the electrostatic induction between the top and bottom electrodes during the lifting up process and is negligible because it is much lower than  $q_1$  and  $q_2$ .

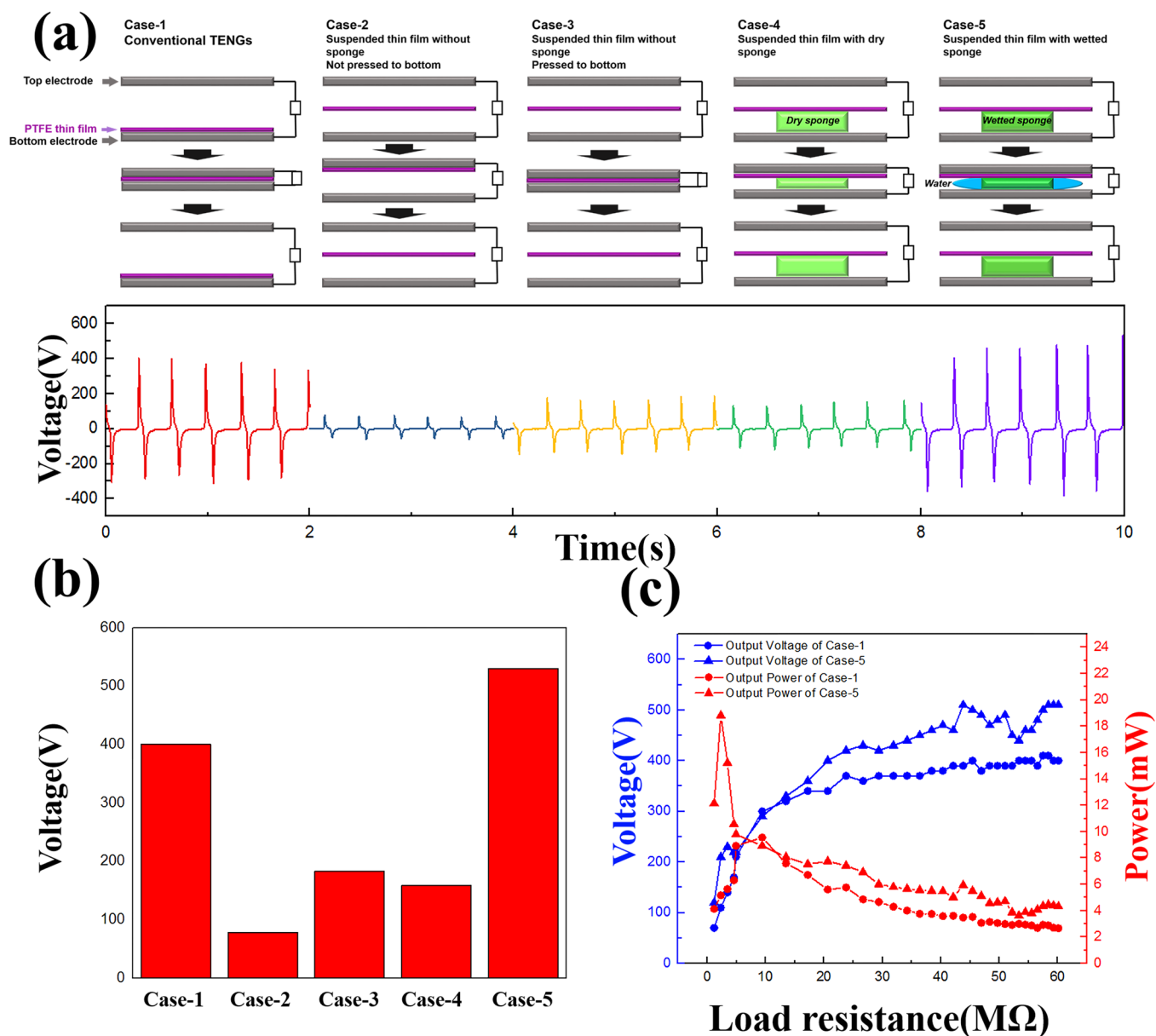
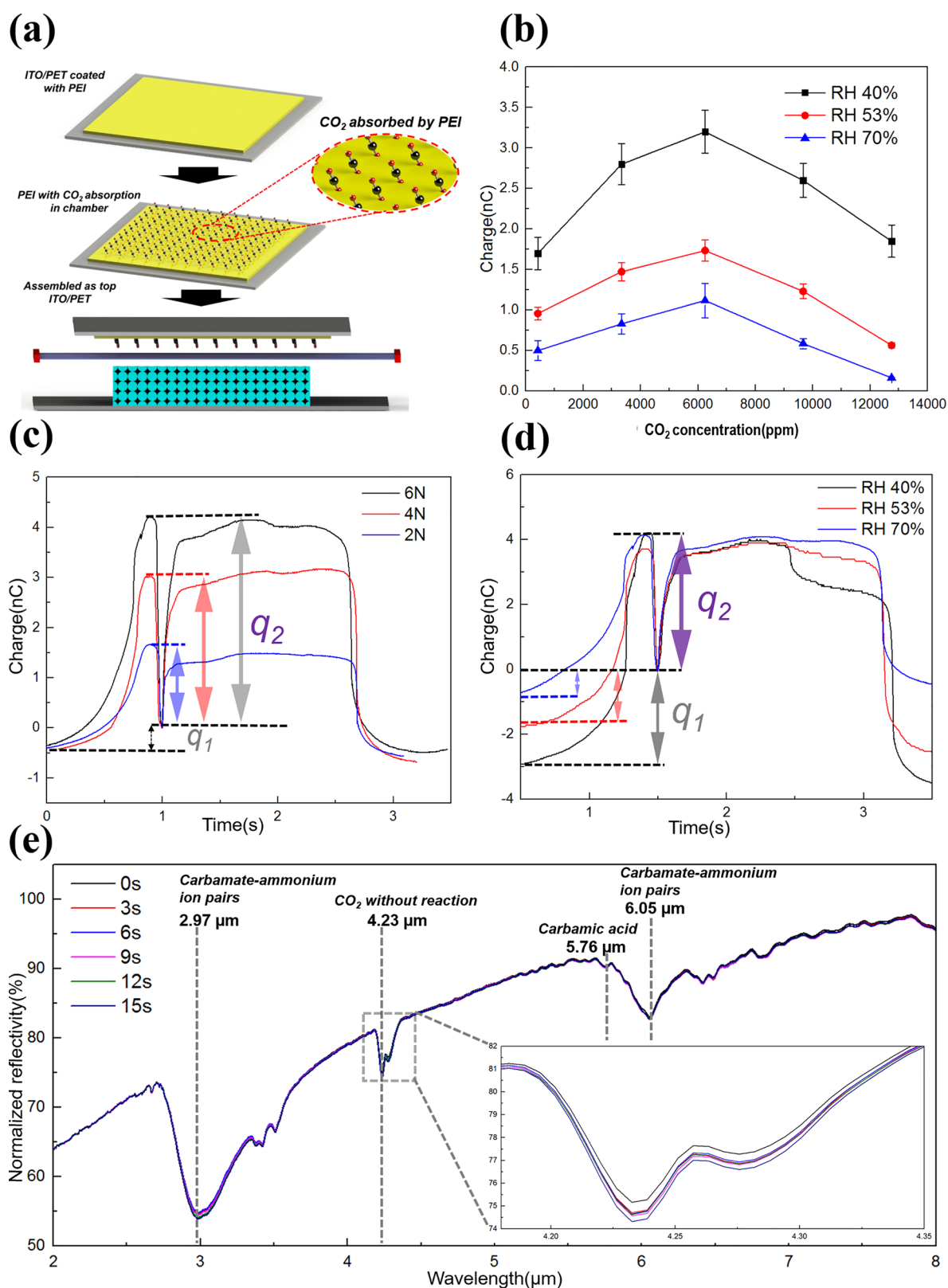


Figure 3. Comparison of the output between different kinds of structures. (a) Different structure and the voltage output with 100 M $\Omega$  load resistance. (b) The average voltage output of the five cases in (a). (c) The output power and voltage characterization of the conventional TENGs (case 1) and WATENG (case 5).

for most cases. Then,  $q_1$  and  $q_2$  can be considered as the charges on the upper and lower surfaces of the PDMS thin film, respectively.

**Analysis of Output Affected by Force and Relative Humidity.** The RH and force are the two major factors that make the performance of TENGs unstable. Although it has been reported that water molecules can help stabilize the charge generated by contact electrification,<sup>41</sup> a higher RH will deteriorate the performance of TENGs in terms of charge<sup>42</sup> and voltage<sup>43</sup> characteristics. Force will affect the contact area, which directly determines the amount of electrostatic charge that participates in electrostatic induction. Here, we made a detailed study of how  $q_1$  and  $q_2$  are affected by RH and force. Figure 2b shows the total charge transferred, which is the sum of  $q_1$  and  $q_2$  at a different force, RH, and water volume inside the sponge. The higher volume of water inside the sponge will have a larger contact area between water and PDMS when the

sponge is squeezed with the same force. When the force is lower than 1.5 N, the total charge for water volume of 1 and 1.75 mL is the same. This means that almost no water was squeezed out from the sponge. When the force is higher than 1.5 N, the charge curve of 1.75 mL is always higher than that of 1 mL because more water was squeezed out of the sponge to induce a larger contact area between water and PDMS. The characterization of  $q_1$  and  $q_2$ , which constitute the total charge in Figure 2b, is shown in Figure 2c,d, respectively. As shown in Figure 2d,  $q_1$  significantly increases when RH decreases. This nonlinear change indicates that the charge output will logarithmically increase with a decrease of RH, which is consistent with the result reported in ref 43, and  $q_1$  remains constant by changing the force. Because the PDMS thin film was suspended by a frame, the top electrode will always fully contact the PDMS upper surface even with a very small pressing force, which results in a constant contact area. In



**Figure 4.** Static characterization of the CO<sub>2</sub>–PEI complexation effect on WATENG performance. (a) Testing procedure. (b) The value of  $q_1$  for different CO<sub>2</sub> concentrations and RH. (c) A group of charge curves at different forces in an ambient environment (RH = 53%, CO<sub>2</sub> concentration = 420 ppm). (d) A group of charge curves with a different RH (force = 6 N; CO<sub>2</sub> concentration = 6250 ppm). (e) Reflective IR spectra of the 0.5 μm-thick PEI coated on a molybdenum substrate that is kept in a chamber with a 2000 ppm of CO<sub>2</sub> concentration for a duration of 3–15 s.

addition, this constant  $q_1$  with different force also confirms that  $q_1$  represents the charge on the upper surface of the PDMS thin

film. Figure 2e shows  $q_2$  as a function of changing RH and force, and  $q_2$  increases with increasing force and remains

constant at different RH. A larger force leads to more water being squeezed out from the sponge and increases the contact area between water and PDMS. Thus, more negative electrostatic charge can be balanced by the electric double layer, which induces a higher  $q_2$ . However, RH has little effect on  $q_2$ . This is because RH of the contact surface between PDMS and water is already at maximum due to the involvement of water. This maximum RH will not be further affected by the change of RH in the ambient environment. A group of charge curves of the samples with 5 N of applied force with different RH is shown in Figure 2f. Although the total transferred charge increases with a decrease of RH,  $q_2$  is the same.

In summary, two main components of the total transferred charge of WATENG, which are  $q_1$  and  $q_2$ , are solely controlled by RH and force, respectively. Thus, based on the calibration, WATENG can be simultaneously used as a sensor for RH and force.

**Characterization of Output Enhancement.** Based on the explanation above, the electrostatic charge on both the upper and lower surfaces of the PDMS thin film is used for generating the output. Apparently, compared with conventional TENGs, in which only the upper surface of the dielectric layer is used for generating output, the structure of the WATENG can generate more electrostatic charge, hence enhancing the output. Here we have a characterization of the output of five different structures of TENGs, including conventional TENGs and WATENG. Considering that PTFE is a more popular material as the dielectric to be used in TENGs for higher energy output,<sup>32,49,50</sup> here we used PTFE thin film instead of PDMS thin film for all the five cases for the comparison of the output.

The structures and the output voltage of the five cases are shown in Figure 3a. Case 1 shows a conventional structure of the TENGs. The PTFE thin film was directly attached onto the bottom electrode. The output voltage was generated by the contact and separation of the top electrode and the upper surface of the PTFE thin film. Cases 2 and 3 show a suspended PTFE thin film structure without a sponge beneath. The suspended PTFE thin film will not contact the bottom electrode during the pressing in case 2 and will have contact with the bottom electrode in case 3. Cases 4 and 5 are the same structure as shown in Figure 2 but with a dry sponge and a wetted sponge, respectively.

The output voltage of case 1, which is 400 V, is lower than that of case 5, which is 530 V, as shown in Figure 3b. This confirms that our structure can achieve a higher output than conventional TENGs structure.

By hard pressing in cases 2 and 3, the suspended thin film contacts the bottom electrode to generate a higher output. This is due to that the lower surface of the suspended thin film contacts the bottom electrode, and the negative electrostatic charge is generated on the lower surface of the thin film. Thus, there will be a similar double side charge coupling during the pressing, hence enhancing the output. However, because of the air gap, which leads to a large inner impedance, the output voltage is much lower compared to case 5.

For case 4, since the sponge is dry, no water can be squeezed out of the sponge. The electrification between the PTFE and sponge cannot be as efficient as either between the water and PTFE or between the PTFE and ITO. Although there is negative charge generated upon the lower surface of the PTFE thin film, the output voltage is still lower than cases 3 and 5.

We also characterize the output power and inner impedance for cases 1 and 5, as shown in Figure 3c, since these two give the best performance. As can be seen, the output voltage of case 5 was always higher than case 1. The maximum output power for case 5 is 15.2 mW at 3.47 M $\Omega$ , while for case 1, it is 9.55 mW at 9.4 M $\Omega$ . The WATENG structure of case 5 can achieve not only higher optimum output power but also a lower matched load resistance.

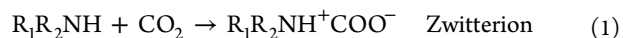
In summary, the developed WATENG structure with a suspended thin film and wetted sponge can enhance the performance compared with a conventional TENG structure. In this research, we did not optimize the material of the suspended thin film. Actually a lot of techniques, including the surface treatment, surface coating, and better material selection, are investigated to enhance the output. The suspended thin-film structure is compatible with all these material optimizations for a better performance.

**Static CO<sub>2</sub> Sensing at Different RH.** To demonstrate the application of WATENG as a CO<sub>2</sub> sensor, a layer of polyethylenimine (PEI) was dip-coated onto the ITO/PET electrode. The PEI is the most commonly used macromolecule for CO<sub>2</sub> adsorbents because of its high amine content in the polymer backbone; primary, secondary, and tertiary amines make up 33% of the total weight.<sup>51</sup> With absorption of CO<sub>2</sub> within PEI, the formation of a carbamate layer, which is a CO<sub>2</sub>-PEI complexation,<sup>52</sup> will change the electronegativity of the PEI surface, which affects the output of WATENG.

Currently, how the CO<sub>2</sub>-PEI complexation affects the WATENG performance remains unknown. A static characterization was conducted to provide detailed investigation. The ITO/PET electrode coated with PEI was kept in a sealed chamber with a controlled CO<sub>2</sub> concentration and RH for 30 min to ensure that the NH-CO<sub>2</sub> production reaction was stable. The test setup can be found in Supplementary S2. Then, we removed the electrode and assembled it on the WATENG for testing, as shown in Figure 4a. Here, we also investigated how  $q_1$  and  $q_2$  were affected. A group of charge curves at ambient environment with different forces is shown in Figure 4c, where  $q_2$  increases with force, while  $q_1$  remains constant. In addition, for the samples that are kept at the same CO<sub>2</sub> concentration, 6250 ppm, with different RH,  $q_1$  decreases with an increase of RH, while  $q_2$  remains constant. The results are consistent with a previous working mechanism analysis. Since the PEI coating only affects the electrification between the upper PDMS layer and the top electrode, which is represented by  $q_1$ , only the change of  $q_1$  was used to characterize the influence of CO<sub>2</sub> absorption in PEI.

In Figure 4b,  $q_1$  is shown under different RH and CO<sub>2</sub> concentrations. For the RH of 40%, which can generate the highest charge transfer,  $q_1$  increases with CO<sub>2</sub> concentration and peaks at 6250 ppm. Then,  $q_1$  drops from 3.2 nC to 1.85 nC when the CO<sub>2</sub> concentration increases from 6250 to 12750 ppm.

The curves of higher RH levels also show the same trend. This nonmonotonous change indicates that there are more than one factor that affect surface electronegativity of the PEI surface. Indeed, the absorption of CO<sub>2</sub> on PEI gives rise to several absorbed species:<sup>53-55</sup> carbamate-ammonium ion pairs, zwitterions, and carbamic acid, as shown below, where R<sub>1</sub>R<sub>2</sub>NH can be a primary or a secondary amine molecule:



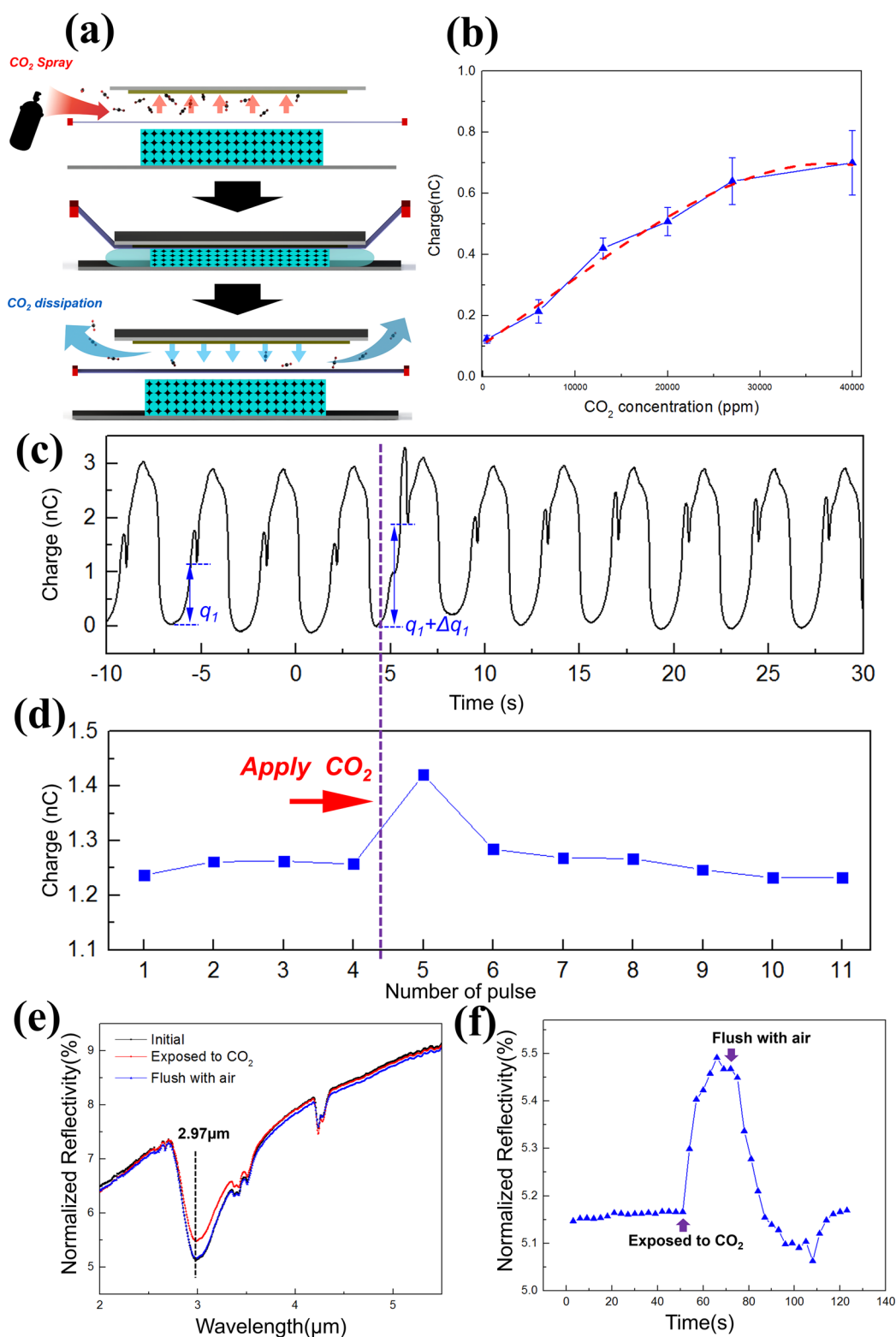
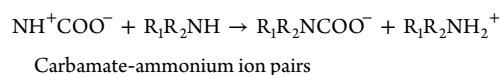
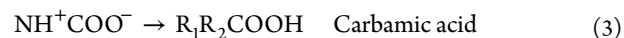


Figure 5. Dynamic CO<sub>2</sub> concentration characterization. (a) Testing procedure. (b) The value of  $\Delta q_1$  with a gas spray of different CO<sub>2</sub> concentrations at an ambient environment. (c) Charge-transfer curve showing the change of  $q_1$  when the PEI surface was blown with a CO<sub>2</sub> spray. (d) The value of  $q_1$  of each pulse in (c). (e) IR spectra of PEI coated on a molybdenum substrate: black line (overlapped with the blue line) is the initial IR spectrum when the chamber is filled with ambient air; the red line is the IR spectrum when the chamber is filled with 2000 ppm of CO<sub>2</sub> gas concentration; and the blue line is the IR spectrum when the chamber is flushed again with ambient air. (f) The normalized reflectivity at 2.97 μm for the entire experiment shown in (e) with a time interval of 3 s.



(2)



Among them, the carboxylic acid production, which is the carbamic acid, can act as an electron donor during the contact electrification with PDMS and becomes positive. Hence, a higher CO<sub>2</sub> concentration, which can increase the production of carbamic acid, will yield a higher  $q_1$ . However, the decrease of  $q_1$  at the CO<sub>2</sub> concentration higher than 6250 ppm indicates that carbamic acid is not the only factor that determines contact electrification upon the surface. A possible reason is that the gaseous CO<sub>2</sub> can be trapped on top and infiltrates through the PEI layer without reacting with PEI. As a nonpolar molecule, the electronegativity of CO<sub>2</sub> is 0, which means that it will not take part in the contact electrification. IR spectra from a previous study show the existence of CO<sub>2</sub> in the PEI layer.<sup>51</sup> To confirm this, reflective IR spectra of the 0.5  $\mu\text{m}$ -thick PEI coated on a molybdenum substrate are acquired with different time durations in the chamber with a 2000 ppm of CO<sub>2</sub> concentration, as shown in Figure 4e. As can be seen, other than carbamate-ammonium ion pairs (2.97 and 6.05  $\mu\text{m}$ ) and carbamic acid (5.67  $\mu\text{m}$ ), the absorption of CO<sub>2</sub> on PEI also resulted in nonreactive CO<sub>2</sub> (4.23  $\mu\text{m}$ ). The amount of nonreactive CO<sub>2</sub> increases with time. Thus, for the situations with CO<sub>2</sub> concentration higher than 6250 ppm, the saturation of reaction between PEI and CO<sub>2</sub> will result in a surface coverage by excessive nonpolar CO<sub>2</sub>, which further inhibits the charge transfer during the contact electrification and causes the drop of  $q_1$  at a higher range of CO<sub>2</sub> concentration. The detailed testing setup for acquiring IR spectra can be found in Supplementary S3.

Since the CO<sub>2</sub> concentration at indoor environment will have a fluctuation from 400 to 2000 ppm, the sensitivity of CO<sub>2</sub> sensing of this range is also calculated based on the testing data in Figure 4b. The sensitivity is  $4.8 \times 10^{-4}$  nC/ppm for 40% RH,  $2.28 \times 10^{-4}$  nC/ppm for 53% RH, and  $1.114 \times 10^{-4}$  nC/ppm for 70% RH. As can be seen, the dry environment can improve the sensitivity of the triboelectric-based sensor.

**Dynamic CO<sub>2</sub> Sensing.** The static characterization only shows the change in  $q_1$  with stabilized CO<sub>2</sub> absorption in the PEI layer. However, the capability of CO<sub>2</sub> sensing in a dynamic air flow will be more important. Here, the dynamic CO<sub>2</sub> sensing in a gas spray, which mimics exhalation, is characterized. The testing procedure is shown in Figure 5a. Before the top electrode is pressed down, a gas spray with a 1000 mL gas volume with different CO<sub>2</sub> concentrations was blown onto the top electrode with a 1 s duration. The gaseous CO<sub>2</sub> will have a temporarily reaction with the PEI surface. Then, the top electrode was pressed down and lifted up, which generates a charge transfer curve. A series of charge-transfer curves for 11 pulses is shown in Figure 5c. The CO<sub>2</sub> spray of 13,000 ppm occurred before the starting point of the fifth pulse. As can be seen, before the CO<sub>2</sub> spray was applied,  $q_1$  was approximately 1.23 nC. Based on the calibration of  $q_1$  at different RH with an ambient CO<sub>2</sub> concentration of 420 ppm in Supporting Information S4, RH can be estimated as 48%. After the CO<sub>2</sub> spray was applied, an increase of  $q_1$  was observed in the fifth pulse. However,  $q_1$  recovered to the normal level after the sixth pulse. The period of the operation cycle is 5 s. Thus, it seems that  $q_1$  can recover within 5 s, and  $q_1$  of each pulse is shown in Figure 5d. The change of  $q_1$ , which is  $\Delta q_1$ , characterizes the CO<sub>2</sub> concentration of the applied gas spray. The value of  $\Delta q_1$  with a CO<sub>2</sub> spray concentration ranging from 420 ppm, which is the concentration of the ambient environment, to 40,000 ppm, which is the CO<sub>2</sub> concentration of exhalation, is shown in Figure 5b, and  $\Delta q_1$  increases with

CO<sub>2</sub> within the entire range. However, the fitting curve indicates that the curve peaks at a concentration between 27,000 and 40,000 ppm, which means that the data point of 40,000 ppm is on the declining trend. The reason is the same as the decrease of  $q_1$  in static characterization. The excessive amount of nonpolar CO<sub>2</sub> molecules covers the surface and reduces the efficiency of contact electrification. An interesting point is that  $\Delta q_1$  can recover to the ambient level in the subsequent pulse after applying the CO<sub>2</sub> spray even when the concentration is very high. This is because the complexation of CO<sub>2</sub> and PEI will inhibit further CO<sub>2</sub> infiltration.<sup>52</sup> The CO<sub>2</sub> trapping and reaction can only occur on the PEI surface during a short-term gas spray. Without CO<sub>2</sub> diffusing into the PEI internal layer, CO<sub>2</sub> can detach from the surface and dissipate very fast. The IR spectra of PEI coated on a molybdenum substrate, which show the change of complexation of CO<sub>2</sub> and PEI for the 2000 ppm of CO<sub>2</sub> gas concentration and ambient environment gas concentration, are shown in Figure 5e. The black line shows the initial IR spectrum when the chamber is filled with ambient air. Then, the chamber is filled with a 2000 ppm of CO<sub>2</sub> gas concentration for 15 s, which is the red line. Then, the chamber is flushed with ambient air again for another 15 s, and the spectrum recovers, which is shown as the blue line. As can be seen, the black and blue lines fully overlap, which indicates a complete recovery. The amplitude of reflectivity at 2.97  $\mu\text{m}$  was recorded with a 3 s time interval, which is the minimum time duration for scanning the IR spectra, for the entire experiment, as shown in Figure 5f. As indicated in the figure, when the sample was exposed to 2000 ppm of CO<sub>2</sub>, the normalized reflectivity began to rise and peaked after 15 s. Then, the chamber was flushed with ambient air for another 15 s. The normalized reflectivity immediately began to drop with almost the same rate of increase. This result shows that the CO<sub>2</sub>-PEI reaction on the surface can be quickly changed by the environment. Since the IR spectra scanning requires at least 3 s, we do not have a chance to further investigate the real recovery time if the gas spray only lasts for 1 s. Considering that in the dynamic CO<sub>2</sub> sensing, the gas spray only lasts for 1 s, the time required for full recovery should also be 1 or 2 s. It should be noted that  $\Delta q_1$  can also be observed for a CO<sub>2</sub> spray at an ambient concentration, which is 420 ppm. In the test, gas was sprayed at a very high flow rate, which is 1000 mL/s. Such high flow rate also increases the chance of contact between CO<sub>2</sub> molecules and PEI surface, which generates more CO<sub>2</sub> and PEI complexation and increases  $\Delta q_1$ . This reveals that the mass flow rate should be the real factor that determines  $\Delta q_1$ .

In summary,  $q_1$  and  $\Delta q_1$ , which are measured during the operation of WATENG, are used to determine RH and the CO<sub>2</sub> concentration, respectively. Considering that RH interferes with the performance of triboelectric output, with a complete calibration of  $\Delta q_1$  versus CO<sub>2</sub> concentration for each RH, as shown in Figure 5b, the WATENG can be used for CO<sub>2</sub> sensing for environments with different RH. Meanwhile, because both the upper and lower surfaces of the dielectric layer are used for electrostatic charge coupling, the output energy of the WATENG can be much enhanced compared with TENGs with conventional structure. With the PEI coating, the CO<sub>2</sub> sensing is characterized at different RH in a static environment. The sensing range can be up to 6000 ppm. A higher CO<sub>2</sub> concentration introduces a nonmonotonous effect and causes a deteriorated sensing result because of the accumulation of excessive CO<sub>2</sub> on the surface. A lower RH

leads to a higher triboelectric output, which offers better sensitivity. Hence, for a continuous CO<sub>2</sub> sensing application, a desiccant, which is used to lower the RH surrounding environment of WATENG, can enhance the responsivity and sensitivity. The dynamic CO<sub>2</sub> sensing of a pulse gas spray is also demonstrated. Compared with the static situation, the sensing range of the dynamic situation can be broadened to 30,000 ppm. The output tends to saturate when the CO<sub>2</sub> concentration is higher than 30,000 ppm. In the dynamic testing, the ambient RH can also be measured when the ambient CO<sub>2</sub> concentration is a constant value, which is approximately 420 ppm. With the characterization of  $q_1$  at a CO<sub>2</sub> concentration of 420 ppm, this dynamic testing manner is useful for the environments with various RH. Thus, the structure of WATENG enables itself as a self-powered amenity sensor.

## ASSOCIATED CONTENT

### Supporting Information

The Supporting Information is available free of charge on the ACS Publications website at DOI: 10.1021/acsnano.7b05213.

S1: Detailed fabrication process, optical and SEM images of the WATENG. S2: Testing chamber to control the humidity, CO<sub>2</sub> concentration for static characterization. S3: Testing setup for obtaining IR spectra. S4: Calibration of  $q_1$  at ambient CO<sub>2</sub> concentration (420 ppm) with different RH (PDF)

## AUTHOR INFORMATION

### Corresponding Author

\*E-mail: [elelc@nus.edu.sg](mailto:elelc@nus.edu.sg).

### Funding

This work was supported by grants from the National Research Foundation (NRF) CRP project 'Self-Powered Body Sensor Network for Disease Management and Prevention Oriented Healthcare' (R-263-000-A27-281), Ministry of Education (MOE) Faculty Research Committee (FRC) grant (R-263-000-B56-112) "Thermoelectric Power Generator (TEG)-Based Self-Powered ECG Plaster – System Integration (Part 3)", HiFES seed fund "Hybrid Integration of Flexible Power Source and Power Sensors" and the National Natural Science Foundation of China under grant no. 61474078 at NUS (Suzhou) Research Institute, Suzhou, China.

### Notes

The authors declare no competing financial interest.

## REFERENCES

- (1) Hoy, M. B. Smart buildings: An Introduction to The Library of The Future. *Med. Ref. Serv. Q* **2016**, *35*, 326–331.
- (2) Abeansinghe, D. C.; Dasgupta, S.; Jackson, H. E.; Boyd, J. T. Boyd. Novel MEMS Pressure and Temperature Sensors Fabricated on Optical Fibers. *J. Micromech. Microeng.* **2002**, *12*, 229.
- (3) Chen, L.-T.; Lee, C.-Y.; Cheng, W.-H. MEMS-Based Humidity Sensor with Integrated Temperature Compensation Mechanism. *Sens. Actuators, A* **2008**, *147*, 522–528.
- (4) Dai, C.-L. A Capacitive Humidity Sensor Integrated with Micro Heater and Ring Oscillator Circuit Fabricated by CMOS–MEMS Technique. *Sens. Actuators, B* **2007**, *122*, 375–380.
- (5) Dai, C.-L.; Liu, M.-C.; Chen, F.-S.; Wu, C.-C.; Chang, M.-W. A Nanowire WO<sub>3</sub> Humidity Sensor Integrated with Micro-Heater and Inverting Amplifier Circuit on Chip Manufactured Using CMOS–MEMS Technique. *Sens. Actuators, B* **2007**, *123*, 896–901.
- (6) Mutschall, D.; Obermeier, E. A Capacitive CO<sub>2</sub> Sensor With On-Chip Heating. *Sens. Actuators, B* **1995**, *25*, 412–414.
- (7) Bang, Y.-I.; Song, K.-D.; Joo, B.-S.; Huh, J.-S.; Choi, S.-D.; Lee, D.-D. Thin Film Micro Carbon Dioxide Sensor Using MEMS Process. *Sens. Actuators, B* **2004**, *102*, 20–26.
- (8) Wang, S.; Lin, L.; Wang, Z. L. Triboelectric Nanogenerators as Self-Powered Active Sensors. *Nano Energy* **2015**, *11*, 436–462.
- (9) Wang, Z. L. Self-Powered Nanosensors and Nanosystems. *Adv. Mater.* **2012**, *24*, 280–285.
- (10) Wang, Z. L. Self-Powered Nanotech. *Sci. Am.* **2008**, *298*, 82–87.
- (11) Wang, Z. L. Triboelectric Nanogenerators as New Energy Technology for Self-Powered Systems and as Active Mechanical and Chemical Sensors. *ACS Nano* **2013**, *7*, 9533–9557.
- (12) Fan, F.-R.; Tian, Z.-Q.; Wang, Z. L. Flexible Triboelectric Generator. *Nano Energy* **2012**, *1*, 328–334.
- (13) Cao, X.; Jie, Y.; Wang, N.; Wang, Z. L. Triboelectric Nanogenerators Driven Self-Powered Electrochemical Processes for Energy and Environmental Science. *Adv. Energy Mater.* **2016**, *6*, 1600665.
- (14) Chen, S. W.; Cao, X.; Wang, N.; Ma, L.; Zhu, H. R.; Willander, M.; Jie, Y.; Wang, Z. L. An Ultrathin Flexible Single-Electrode Triboelectric-Nanogenerator for Mechanical Energy Harvesting and Instantaneous Force Sensing. *Adv. Energy Mater.* **2017**, *7*, 1601255.
- (15) Xi, Y.; Guo, H.; Zi, Y.; Li, X.; Wang, J.; Deng, J.; Li, S.; Hu, C.; Cao, X.; Wang, Zhong Lin Multifunctional TENG for Blue Energy Scavenging and Self-Powered Wind-Speed Sensor. *Adv. Energy Mater.* **2017**, *7*, 1602397.
- (16) Chen, S.; Wang, N.; Ma, L.; Li, T.; Willander, M.; Jie, Y.; Cao, X.; Wang, Z. L. Triboelectric Nanogenerator for Sustainable Wastewater Treatment via a Self-Powered Electrochemical Process. *Adv. Energy Mater.* **2017**, *6*, 1501778.
- (17) Li, T.; Xu, Y.; Xing, F.; Cao, X.; Bian, J.; Wang, N.; Wang, Z. L. Boosting Photoelectrochemical Water Splitting by TENG-Charged Li-Ion Battery. *Adv. Energy Mater.* **2017**, *7*, 1700124.
- (18) Jiang, J.; Wang, M.; Yan, W.; Liu, X.; Liu, J.; Yang, J. and Licheng Sun. Highly Active and Durable Electrocatalytic Water Oxidation by a NiB<sub>0.45</sub>/NiO<sub>x</sub> Core-Shell Heterostructured Nanoparticulate Film. *Nano Energy* **2017**, *38*, 175–184.
- (19) Yu, A.; Jiang, P.; Wang, L. Z. Nanogenerator as Self-powered Vibration Sensor. *Nano Energy* **2012**, *1*, 418–423.
- (20) Lin, L.; Xie, Y.; Wang, S.; Wu, W.; Niu, S.; Wen, X.; Wang, Z. L. Triboelectric Active Sensor Array for Self-Powered Static and Dynamic Pressure Detection and Tactile Imaging. *ACS Nano* **2013**, *7*, 8266–8274.
- (21) Fan, F.-R.; Lin, L.; Zhu, G.; Wu, W.; Zhang, R.; Wang, Z. L. Transparent Triboelectric Nanogenerators and Self-Powered Pressure Sensors Based on Micropatterned Plastic Films. *Nano Lett.* **2012**, *12*, 3109–3114.
- (22) Zhu, G.; Yang, W. Q.; Zhang, T.; Jing, Q.; Chen, J.; Zhou, Y. S.; Bai, P.; Wang, Z. L. Self-Powered, Ultrasensitive, Flexible Tactile Sensors Based on Contact Electrification. *Nano Lett.* **2014**, *14*, 3208–3213.
- (23) Yang, Y.; Zhang, H.; Lin, Z.-H.; Zhou, Y. S.; Jing, Q.; Su, J.; Yang, J.; Hu, C.; Wang, Z. L. Human Skin Based Triboelectric Nanogenerators for Harvesting Biomechanical Energy and as Self-Powered Active Tactile Sensor System. *ACS Nano* **2013**, *7*, 9213–9222.
- (24) Meng, B.; Tang, W.; Too, Z.-h.; Zhang, X.; Han, M.; Liu, W.; Zhang, H. A Transparent Single-Friction-Surface Triboelectric Generator and Self-Powered Touch Sensor. *Energy Environ. Sci.* **2013**, *6*, 3235–3240.
- (25) Yang, Y.; Zhang, H.; Zhong, X.; Yi, F.; Yu, R.; Zhang, Y.; Wang, Z. L. Electret Film-Enhanced Triboelectric Nanogenerator Matrix for Self-Powered Instantaneous Tactile Imaging. *ACS Appl. Mater. Interfaces* **2014**, *6*, 3680–3688.
- (26) Gupta, R. K.; Shi, Q.; Dhakar, L.; Wang, T.; Heng, C. H.; Lee, C. Broadband Energy Harvester Using Non-linear Polymer Spring and Electromagnetic/Triboelectric Hybrid Mechanism. *Sci. Rep.* **2017**, *7*, 41396.

- (27) Yang, W.; Chen, J.; Wen, X.; Jing, Q.; Yang, J.; Su, Y.; Zhu, G.; Wu, W.; Wang, Z. L. Triboelectrification Based Motion Sensor for Human-Machine Interfacing. *ACS Appl. Mater. Interfaces* **2014**, *6*, 7479–7484.
- (28) Zhang, L.; Xue, F.; Du, W.; Han, C.; Zhang, C.; Wang, Z. Transparent Paper-Based Triboelectric Nanogenerator as a Page Mark and Anti-Theft Sensor. *Nano Res.* **2014**, *7*, 1215–1223.
- (29) Bai, P.; Zhu, G.; Jing, Q.; Yang, J.; Chen, J.; Su, Y.; Ma, J.; Zhang, G.; Wang, Z. L. Membrane-Based Self-Powered Triboelectric Sensors for Pressure Change Detection and Its Uses in Security Surveillance and Healthcare Monitoring. *Adv. Funct. Mater.* **2014**, *24*, 5807–5813.
- (30) Lin, L.; Wang, S.; Xie, Y.; Jing, Q.; Niu, S.; Hu, Y.; Wang, Z. L. Segmentally Structured Disk Triboelectric Nanogenerator for Harvesting Rotational Mechanical Energy. *Nano Lett.* **2013**, *13*, 2916–2923.
- (31) Lin, L.; Wang, S.; Niu, S.; Liu, C.; Xie, Y.; Wang, Z. L. Noncontact Free-rotating Disk Triboelectric Nanogenerator as a Sustainable Energy Harvester and Self-Powered Mechanical Sensor. *ACS Appl. Mater. Interfaces* **2014**, *6*, 3031–3038.
- (32) Yang, Y.; Zhang, H.; Chen, J.; Jing, Q.; Zhou, Y. S.; Wen, X.; Wang, Z. L. Single-Electrode-Based Sliding Triboelectric Nanogenerator for Self-Powered Displacement Vector Sensor System. *ACS Nano* **2013**, *7*, 7342–7351.
- (33) Wang, H.; Xiang, Z.; Giorgia, P.; Mu, X.; Yang, Y.; Wang, Z. L.; Lee, C. Triboelectric Liquid Volume Sensor for Self-Powered Lab-On-Chip Applications. *Nano Energy* **2016**, *23*, 80–88.
- (34) Shi, Q.; Wang, H.; Wang, T.; Lee, C. Self-Powered Liquid Triboelectric Microfluidic Sensor for Pressure Sensing and Finger Motion Monitoring Applications. *Nano Energy* **2016**, *30*, 450–459.
- (35) Lin, Z.-H.; Zhu, G.; Zhou, Y. S.; Yang, Y.; Bai, P.; Chen, J.; Wang, Z. L. A Self-Powered Triboelectric Nanosensor for Mercury Ion Detection. *Angew. Chem., Int. Ed.* **2013**, *52*, 5065–5069.
- (36) Lin, Z.-H.; Xie, Y.; Yang, Y.; Wang, S.; Zhu, G.; Wang, Z. L. Enhanced Triboelectric Nanogenerators and Triboelectric Nanosensor Using Chemically Modified TiO<sub>2</sub> Nanomaterials. *ACS Nano* **2013**, *7*, 4554–4560.
- (37) Zhang, H.; Liu, F.; Phanikumar, M. S.; Meerschaert, M. M. Meerschaert. A Novel Numerical Method for the Time Variable Fractional Order Mobile-Immobile Advection-Dispersion Model. *Comput. Math. Appl.* **2013**, *66*, 693–701.
- (38) Lin, Z.-H.; Cheng, G.; Wu, W.; Pradel, K. C.; Wang, Z. L. Dual-Mode Triboelectric Nanogenerator for Harvesting Water Energy and as a Self-Powered Ethanol Nanosensor. *ACS Nano* **2014**, *8*, 6440–6448.
- (39) Lin, Z.-H.; Cheng, G.; Yang, Y.; Zhou, S.; Lee, S.; Wang, Z. L. Triboelectric Nanogenerator as an Active UV Photodetector. *Adv. Funct. Mater.* **2014**, *24*, 2810–2816.
- (40) Uddin, A. S. M. I.; Chung, G.-S. Wide-Ranging Impact-Competent Self-Powered Active Sensor Using a Stacked Corrugated-Core Sandwich-Structured Robust Triboelectric Nanogenerator. *Sens. Actuators, B* **2017**, *245*, 1–10.
- (41) Baytekin, H. T.; Baytekin, B.; Soh, S.; Grzybowski, B. A. Grzybowski. Is Water Necessary for Contact Electrification? *Angew. Chem., Int. Ed.* **2011**, *50*, 6766–6770.
- (42) Nguyen, V.; Yang, R. Effect of Humidity and Pressure on the Triboelectric Nanogenerator. *Nano Energy* **2013**, *2*, 604–608.
- (43) Zhang, H.; Yang, Y.; Su, Y.; Chen, J.; Hu, C.; Wu, Z.; Liu, Y.; Wong, C. P.; Bando, Y.; Wang, Z. L. Triboelectric Nanogenerator as Self-Powered Active Sensors for Detecting Liquid/Gaseous Water/Ethanol. *Nano Energy* **2013**, *2*, 693–701.
- (44) Hodgkinson, J.; Smith, R.; Ho, W. O.; Saffell, J. R.; Tatam, R. P. A Low Cost, Optically Efficient Carbon Dioxide Sensor Based on Non-Dispersive Infra-Red (NDIR) Measurement at 4.2  $\mu\text{m}$ . *Proc. SPIE* **2012**, *8439*, 843919.
- (45) Hodgkinson, J.; Tatam, R. P. Tatam. Optical Gas Sensing: A Review. *Meas. Sci. Technol.* **2013**, *24*, 012004.
- (46) Willa, C.; Yuan, J.; Niederberger, M.; Koziej, D. When Nanoparticles Meet Poly (Ionic Liquid) s: Chemoresistive CO<sub>2</sub> Sensing at Room Temperature. *Adv. Funct. Mater.* **2015**, *25*, 2537–2542.
- (47) Endres, H.-e.; Hartinger, R.; Schwaiger, M.; Gmelch, G.; Roth, M. A Capacitive CO<sub>2</sub> Sensor System with Suppression of the Humidity Interference. *Sens. Actuators, B* **1999**, *57*, 83–87.
- (48) Zhou, R.; Schmeisser, D.; Göpel, W. Mass Sensitive Detection of Carbon Dioxide by Amino Group-Functionalized Polymers. *Sens. Actuators, B* **1996**, *33*, 188–193.
- (49) Yang, Y.; Zhou, Y. S.; Zhang, H.; Liu, Y.; Lee, S.; Wang, Z. L. A Single-Electrode Based Triboelectric Nanogenerator as Self-Powered Tracking System. *Adv. Mater.* **2013**, *25*, 6594–6601.
- (50) Zhong, J.; Zhong, Q.; Fan, F.; Zhang, Y.; Wang, S.; Hu, B.; Wang, Z. L.; Zhou, J. Finger Typing Driven Triboelectric Nanogenerator and Its Use for Instantaneously Lighting Up LEDs. *Nano Energy* **2013**, *2*, 491–497.
- (51) Moumen, S.; Raible, I.; Krauß, A.; Wöllenstein, J. Infrared Investigation of CO<sub>2</sub> Sorption by Amine Based Materials for the Development of a NDIR CO<sub>2</sub> Sensor. *Sens. Actuators, B* **2016**, *236*, 1083–1090.
- (52) Zhao, J.; Simeon, F.; Wang, Y.; Luo, G.; Hatton, T. A. Polyethylenimine-Impregnated Siliceous Mesocellular Foam Particles as High Capacity CO<sub>2</sub> Adsorbents. *RSC Adv.* **2012**, *2*, 6509–6519.
- (53) Hahn, M. W.; Steib, M.; Jentys, A.; Lercher, J. A. Mechanism and Kinetics of CO<sub>2</sub> Adsorption on Surface Bonded Amines. *J. Phys. Chem. C* **2015**, *119*, 4126–4135.
- (54) Wilfong, W. C.; Srikanth, C.; Chuang, S. S. *In situ* ATR and DRIFTS Studies of the Nature of Adsorbed CO<sub>2</sub> on Tetraethylenepentamine Films. *ACS Appl. Mater. Interfaces* **2014**, *6*, 13617–13626.
- (55) Wang, X.; Schwartz, V.; Clark, J. C.; Ma, X.; Overbury, S. H.; Xu, X.; Song, C. Infrared Study of CO<sub>2</sub> Sorption over Molecular Basket Sorbent Consisting of Polyethylenimine-Modified Mesoporous Molecular Sieve. *J. Phys. Chem. C* **2009**, *113*, 7260–7268.